Assessing the photoelectrochemical properties of C, N, F codoped TiO$_2$ nanotubes of different lengths

Athanasios Chatzitakis,[1] Mathieu Grandcolas,[2] Kaiqi Xu,[1] Sen Mei,[2] Juan Yang,[2] Ingvild Julie Thue Jensen,[2] Christian Simon,[2] Truls Norby,[1*]

(1) University of Oslo, Department of Chemistry, Centre for Materials Science and Nanotechnology, Oslo, Norway.

(2)Materials and Nanotechnology, SINTEF Materials and Chemistry, Oslo, Norway.

*corresponding author: truls.norby@kjemi.uio.no

Abstract

The aim of this work has been the photoelectrochemical (PEC) study of nanostructured photoanodes based on TiO$_2$. Highly ordered and well adhered TiO$_2$ nanotubes (TNTs) of different lengths (~2-20 μm) were prepared in a two-step process in ethylene glycol solutions containing fluorides, and detailed XPS analysis showed that they have become co-doped with C, N and F. PEC measurements revealed that increasing surface area is not followed by increase in the photoconversion efficiency, but rather that an optimal balance between electroactive surface area (ESA) and charge carrier concentration exists. TNTs of around 10 μm show the optimum incident photon-to-current efficiency of ~33% and an overall photoconversion efficiency of ~6.3% under UV illumination of 4 mW cm^{-2} light intensity. Finally, Mott-Schottky analysis revealed significant frequency dispersion of the estimated space charge layer capacitance, which renders the accurate estimation of the flatband position and charge carrier concentration unreliable. On the other hand, more realistic charge carrier concentrations can be obtained by normalizing the capacitance per ESA.

1. Introduction

Tubular nanostructured titania is a versatile material and has generated great interest for its potential use in practically every field where TiO_2 nanoparticles are already used, including photocatalysis [1], photoelectrolysis [2], dye-sensitised solar cells (DSSCs) [3], gas sensors [4], ion-insertion devices (electrochromism, batteries) [5], biocompatible [6] and self-cleaning materials [7]. The formation of TiO_2 nanotubes is achieved through a strikingly simple synthesis route [8] and the first report on self-organized TiO_2 nanotubes is presented by Zwilling et al. [9] in 1999. At the same time, another advantage of the anodic oxidation process is that the nanotube dimensions are easily controllable by the electrolyte composition and anodization conditions [10]. The one-dimensional nanostructures aligned perpendicular to the substrate, provide a unidirectional electric channel for electron transport, thus improved charge-collection efficiencies and slower recombination rates have been suggested [11, 12].

Compared to anodized aluminium oxide, where the chemical composition and incorporation of electrolyte species within the anodic film have been intensively studied [13], the formation of highly ordered TiO_2 nanotubes-arrays is a rather new field and electrolyte contamination has yet to be investigated. This is particularly interesting in the case of the third generation TiO_2 nanotubes, where the introduction of organic electrolytes allowed the formation of smooth, uniformly shaped, significantly long and of high aspect ratio nanotubes [14, 15]. The electrolysis bath consists of ethylene glycol or glycerol along with small contents of water and fluoride ions, the latter usually from ammonium salts. Thus, there is a significant source of C, N and F species that could possibly be incorporated into the structure of the oxide. Moreover, the tendency for the oxide formation is reduced because the oxygen donation becomes more difficult on the anode electrode [10].

As the incorporation of such dopants can introduce additional energy states in the band gap, thus leading to a band-narrowing, there is a vast number of reports related to such band-gap engineering [16-18]. On the other hand, the primary preparation conditions are rarely investigated in terms of the *in-situ* contamination of the grown nanostructured oxide TiO_2 films. In this work, the chemical composition of TiO_2 nanotubes (TNTs) grown in a two-step process is investigated by means of X-ray photoelectron spectroscopy (XPS), which provides useful

insight. Furthermore, the semiconducting properties of nanotubes are fundamentally related to their chemical composition and for this reason the photoelectrochemical (PEC) performance of TNTs of different length is assessed by i) photocurrent measurements, with corresponding photoconversion efficiencies, under photovoltammetry, and ii) the capacitance dependence from the angular frequency of the AC-perturbation signal ω, by means of Mott-Schottky measurements. In this case, the determination of the flat-band potential and the free carrier concentration may be hampered due to the nano-porous nature of the material. This suggests that estimating the exact energy position of the Fermi level of the electrons, which is closely related to the donor density (for an n-type semiconductor), can be problematic, but potentially facilitated by novel approaches of impedance spectroscopy.

2. Experimental

2.1 Chemicals

Ti foil (0.25 mm thick, 99.7% purity) was purchased from Sigma-Aldrich. Ethylene glycol (EG), ammonium fluoride (NH_4F), isopropanol (i-prop), acetone (Ac) and anhydrous sodium sulfate (Na_2SO_4) were all of analytical grade from Sigma-Aldrich. Deionized water (18.2 MΩ cm) was used throughout the work. All chemicals were used as received without further purification.

2.2 TiO_2 nanotubes preparation

C-, N-, and F-codoped TiO_2 nanotubes (TNTs) were grown in a two-step process. In the first step, the previously cleaned Ti foil of 1 cm^2 surface area (30 min ultrasonication in isopropanol followed by 30 min in acetone) was anodized in an ethylene glycol electrolyte, containing 0.25% wt NH_4F and 2% wt H_2O. The electrochemical anodization was performed in a two-electrodes configuration, where Ti foils were used for both anode and cathode and kept at a

distance of 2 cm. The anodization voltage of the first step was 60 V supplied by a programmable DC power supply (Keithley Instruments Model 2200-72-1DC) for 2 hours at room temperature. Then, the anode was rinsed with water and left to dry vertically in air. While drying, the nanotubes film peeled off spontaneously and a shiny Ti surface was revealed. It should be noted that the stripping of the TNTs film, while the intratubular water/electrolyte volatilizes, hampers their widespread applications. Zhao et al. [19] proposed that the stripping mechanism is due to hydrogen-assisted cracking. The same research team reported that post-treatment of the TNTs in organic solvents of low polarity (petroleum ether, cyclohexane) increased dramatically their adhesion to the Ti substrate. Here, the TNTs layer grown in the second anodization step was left in the anodization solution for 1 h. Although the relative polarity of ethylene glycol compared to water is 0.79 and cyclohexane's 0.006, the adhesion of the film was improved drastically. The cause and mechanism is however beyond the scope of this work. The length of the TNTs was controlled by the anodization time of the second step (5, 20, 30, 45, 60, 90 minutes), which was performed in the same, but fresh solution, voltage and electrochemical configuration. TNTs of the different anodization times and lengths are denoted as TNTs5, TNTs20, TNTs30, TNTs45, TNTs60 and TNTs90. After the post-treatment process, all electrodes were annealed at 500 °C for 2 h with heating rate of 2 °C min^{-1}, in a muffle furnace to obtain the anatase phase. All electrodes were placed inside an alumina crucible with an alumina cover to avoid particle contamination from the furnace.

2.3 Characterization

The morphological characterization of the TNTs was observed with top-view and cross-sectional scanning electron microscopy (SEM) using a FEI Quanta 200F FEG-ESEM microscope. The crystalline phase of the films was determined by X-ray diffraction (XRD) in a Bruker D8 Discover diffractometer using Cu Kα-filtered radiation (λ=1.5406 Å), step 0.02° (2θ), while count time was 10 s/step. The chemical composition of the films was characterized by X-ray photoelectron spectroscopy (XPS) using a Kratos Axis Ultra^{DLD} spectrometer, with

monochromated Al Kα radiation (hν = 1486.6 eV). High resolution spectra were measured using step size 0.1 eV and pass energy 20 eV. In order to remove any surface contaminants and characterize the chemical composition underneath the surface, sputtering was done using an Ar$^+$ ion beam of 0.5 kV or 2 kV delivering 100 µA of current. Due to the 3D-structure of the sample surface a rotating sample holder was used to promote even sputtering. The energy axis was calibrated by using the position of the Ti 2p component of Ti$_2$O (anatase) at 458.6 eV [20]. The photoelectrochemical characterization was performed in a three-electrode electrochemical cell of 25 mL capacity equipped with a quartz window. A light source, Omnicure S2000 UV-vis, with light intensity of 4 mW cm^{-2} was placed at 25.7 cm away from the electrode's surface. The light source was equipped with a filter in the 320 – 500 nm range and the light intensity was calibrated as described elsewhere [21]. Pt foil and saturated calomel electrode (SCE) were used as counter and reference electrodes, respectively. The supporting electrolyte was a 0.5 M Na$_2$SO$_4$ solution (pH=5.6). The photo-electrodes were activated by scanning between the hydrogen and oxygen evolution potentials with a scan rate of 1V s^{-1} for at least 10 cycles in the dark. The applied potential was obtained using the potentiostat PARSTAT 2273 (Princeton Applied Research) equipped with a built-in frequency response analyzer.

All voltages reported were calculated vs. the reversible hydrogen electrode (RHE) using equation 1:

$$E_{RHE} = E_{SCE} + 0.059pH + E^0_{SCE} = E_{SCE} + 0.330 + 0.242 = E_{SCE} + 0.572 \tag{1}$$

3. Results and discussion

3.1 Microscopic (SEM) and crystallographic (XRD) characterization of the TNTs

Figs.1(a, b, c) show typical cross-sectional and top-view SEM micrographs of selected TNTs, while Fig.1d shows the dependence of the nanotubes length on the anodization time. All nanotubes appear smooth and vertically oriented as expected from EG based solutions, and arranged in a closed-pack morphology, which is a common feature for two-step nanotubes [22].

5

A uniform coverage is obtained and their top surface is clean and free of any hydrous titanium impurities [10] or "nanograss" features [23], which are usually observed in this generation of nanotubes, due to the hydrolysis of TiO_2 during anodization and over-etching, respectively. The morphological parameters of the nanostructured TiO_2 are summarized in Table 1.

Table 1: Average geometrical and lattice parameters of TNTs of different lengths. Wall thickness is defined as the solid phase between two pores.

	Tube length (µm)	Inner pore diameter ±10% (nm)	Wall thickness ±10% (nm)	Aspect ratio	Roughness factor	Lattice parameters (Å)	
						a	c
TNTs5	2.14	46	52	~22:1	~117	3.7840	9.506
TNTs20	7.35	70	44	~64:1	~378	3.7835	9.505
TNTs30	10.30	76	23	~104:1	~668	3.7880	9.502
TNTs45	17.20	84	26	~156:1	~1001	3.7786	9.490
TNTs60	20.85	84	30	~183:1	~1153	3.7897	9.513
TNTs90	21.50	90	25	~187:1	~1209	3.7878	9.513

It is evident that with increasing anodization time there is an increase in the length and the aspect ratio (length-to-outer pore diameter), and therefore the roughness factor of the nanotubes. Practically, anodization time of 60 min resulted in nanotubes of maximum length and roughness factor. TNTs of 120 min have also been attempted, but they collapsed in the subsequent heat treatment in order to induce crystallization. The roughness factor is a measure of the geometrical surface area of the nanotubes and it is proposed that the TNTs60 sample has the highest surface area. Further anodization to 90 min did not induce significant change in the surface area, and the roughness factor is within the experimental error. These results are further correlated with the electrochemical measurements obtained with cyclic voltammetry that are presented in section 3.3.
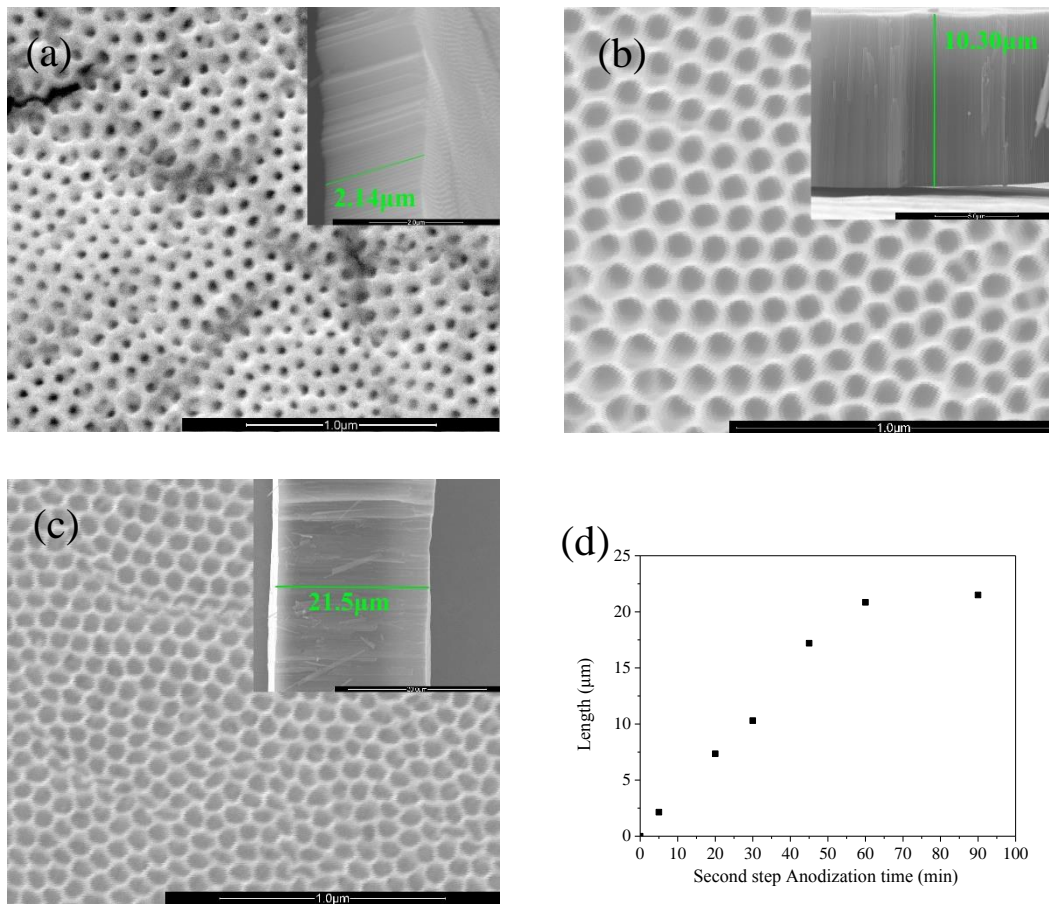
Figure 1: SEM micrographs of TNTs5 (a), TNTs30 (b) and TNTs90 (c), with their corresponding cross-section in the inset. Nanotubes length vs. the anodization time as applied in the second step (d).

It is reported that the anatase phase has 4 orders of magnitude higher electron mobility than the rutile or amorphous material [24]. Anatase is preferred in charge separation devices (PEC, DSSCs) and photocatalysis, while rutile is mostly used in gas sensors and as dielectric layer [25, 26]. Here, XRD analysis showed that after annealing at 500 °C for 2 h, all synthesized TNTs formed primarily the anatase phase.
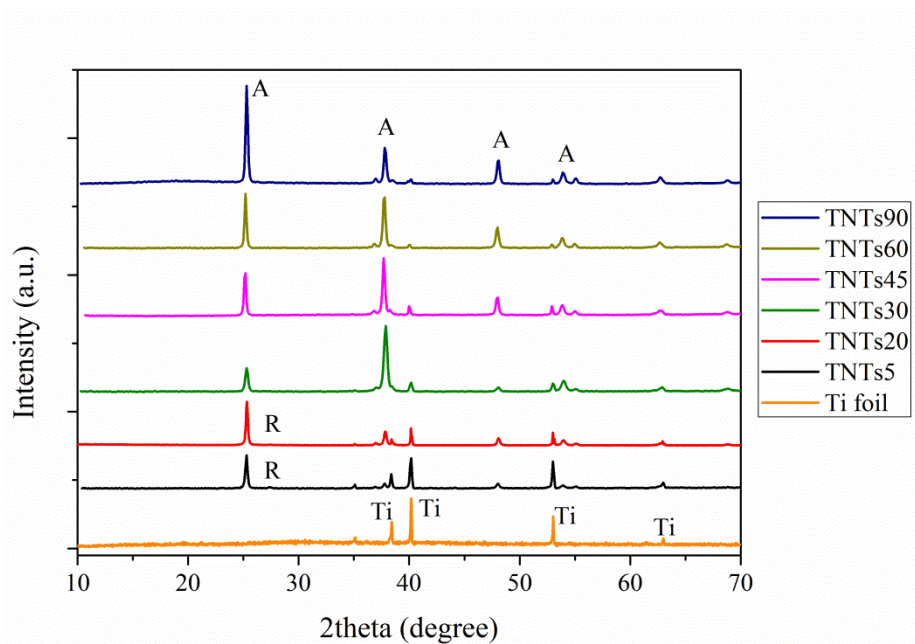
Figure 2: XRD diffractograms of TNTs electrodes of different lengths after annealing at 500 °C.

This is shown in Fig.2, where the TiO_2 anatase peaks of the diffraction diagrams are indexed according to the ICDD-JCPD file 21-1272. It can also be seen that a small rutile (2θ 27.6, ICDD-JCPD 21-1276) fraction is present in the shorter TNTs5 and TNTs20, which for longer TNTs (> ~10 μm) disappears. This is in agreement with the work of Albu et al. [27], who detected the rutile phase in the shorter nanotubes (4.3 μm), but not in the thicker layers (9 and 30 μm). It is implied that the penetration depth of the XRD measurement was around 9 μm, which is probably the reason for not detecting the rutile phase, as expected on the oxide barrier layer between the nanotubes and the substrate. Presently, diffraction peaks from the substrate are detected even for the thickest layer (~21 μm), but rutile is not detected after the TNTs30 sample with thickness of ~10 μm. The rutile phase in the barrier oxide layer will have an impact on the electric properties of the nanostructure, as it has lower electron mobility, but it seems that it is avoided in the growth and annealing conditions chosen for this work. The lattice parameters were calculated with the Rietveld refinement and are presented in Table 1. Data are lacking for an undoped sample, as it will be explained later in the XPS analysis, but the lattice parameters resemble the values of the anatase crystal [28, 29]. It has been reported that in the

case of N substitutionally doped in TiO$_2$ the c value increased (undoped: 9.4449 Å, N-doped: 9.5130 Å, C,N-doped: 9.5259 Å) [30], while in the case of C the crystallite size decreased together with the intensity of the peak (1 0 1), indicating that the incorporation of such atoms suppresses the growth of the crystal and affects crystallinity [31]. On the other hand, lattice deformation in nanoscale oxides can be induced as a result of non-stoichiometry and/or strain effects. Therefore, the XRD results are inconclusive as to whether those atoms substitute O in the lattice of TiO$_2$ [29, 32]. Neutron diffraction may be a better choice to study the location of light atoms such as N, C and F.

3.2. Chemical composition of the TNTs

The film composition and chemical character of the prepared samples were analyzed by XPS using Ar$^+$ sputtering, in order to probe deeper into the samples. The XPS analysis corresponds to results obtained from the TNTs5 and TNTs20 samples, which were similar. Before sputtering, all samples mainly contain Ti, O, and C, and smaller amounts of N and F.
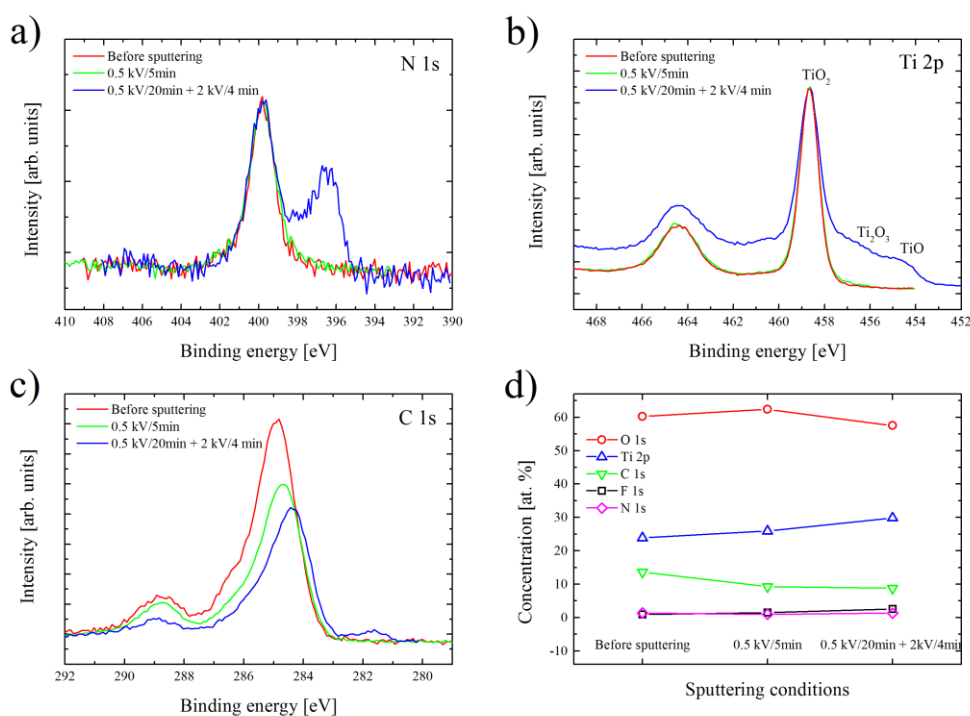
Figure 3: High resolution spectra of the N 1s (a), Ti 2p (b) and C 1s (c) region before and after sputtering. Quantification of sample content based on XPS spectra (d). The spectra shown for 0.5 kV/5 min and 0.5 kV/20 min + 2 kV/4 min are representative for all measured sputtering steps at 0.5 kV and 2 kV, respectively.

For C and N there is general disagreement among researchers on whether the observation of these elements in XPS analysis should be assigned to successful anion doping [33-35], but there is a consensus that C and N peaks at lower binding energies (about 397 eV) arise from occupation of anionic sites in titania [16, 36]. In a recent publication by Mazierski et al. [37], the N 1s signal at 400.7 eV is assigned to doping in the form of O-Ti-N and/or Ti-O-N, and a number of relevant works are cited. On the other hand, Varghese et al. [26, 38] repeatedly points out that substitutional N doping is evidenced with N 1s peaks at binding energies of about 397 eV. Many researchers use Ar^+ sputtering in order to remove surface contaminants and study the chemical composition underneath the surface [35, 38, 39]. A general problem is that XPS results of undoped samples are omitted or not given, as the absence of these peaks is implied. In the present case, the sputtering of the samples was first tested at 0.5 kV in steps up to 20 min, followed by sputtering at 2 kV for 4 minutes. As seen in the high resolution spectra of the N 1s peak in Fig.3a, a component at lower binding energies (~397 eV) appears after exposure to 2 kV sputtering. This component has previously been identified as contribution from substitutional N and is frequently used as a sign of successful N-doping. However, the appearance of the substitutional N component is accompanied by a change in the Ti 2p spectra, see Fig.3b. After exposure to 2 kV sputtering, a shoulder at lower binding energy appears in both the $2p^{1/2}$ and $2p^{3/2}$ regions, corresponding to Ti_2O_3 and TiO, which can be attributed to preferential sputtering of O in TiO_2 [40]. This means that the sputtering itself creates oxygen deficiency leading to the formation of lower oxides, which causes the transformation of interstitially placed N to substitutional N [25, 41]. The same effect can be seen for the C doping as well (Fig.3c), although less pronounced. The main peak around 285 eV is assigned to

adventitious carbon (C-C). Peaks at lower binding energies (282-283 eV) have been assigned to substitutional C species [35, 36], which our analysis attributes to the sputtering process itself. The peaks at 289 and 286.5 eV are usually assigned to C=O and C-O species [34], respectively, therefore we suggest that C is incorporated interstitially in the TiO_2 lattice. Some variations in peak positions originating from differential sample charging are also observed in the C 1s spectra. In our experiment with a rotating XPS sample holder, no changes in the Ti 2p, N 1s and C 1s spectra were observed for sputtering at 0.5 kV (up to 20 minutes), while additional sputtering at 2 kV for 2 and 4 minutes revealed clear changes as discussed above. A more detailed study is needed in order to clarify whether sputtering at 0.5 kV is low enough to avoid preferential sputtering or if it was just an effect of the rotation of the sample reducing the impact, i.e., decreasing the sputtering speed. Comparison to earlier reports [34] may suggest the latter.

In the case of F, it is clear that its peak intensity increases upon sputtering, because fluoride atoms migrate at double the rate of oxygen ions [42] and are incorporated in the anodic film from the electrolyte. Its peak at 685 eV (not shown) suggests the presence of the hexafluorotitanate complex $[TiF_6]^{2-}$ [43] and that the annealing treatment did not induce the complete removal of the fluorine content. Quantitative analysis of the peaks is displayed in Fig.3d, revealing i) the less oxygen rich oxide, ii) the increasing F concentration, iii) the non-exclusively contaminating nature of C and iv) the stability in N content. Our findings suggest that TiO_2 nanotubes prepared in EG solutions of low water content and NH_4F, annealed at 500 ºC for 2h, are co-doped with C and N species, which are most probably placed interstitially in the lattice, while the F species are found in the form of the hexafluorotitanate complex. This suggests the need for a careful examination and difficulty in controlling their chemical composition. The preferential sputtering of oxygen in TiO_2 makes XPS after Ar^+ sputtering unreliable as a means to distinguish between interstitially and substitutionally placed N and C.

3.3 Photoelectrochemical characterization of TNTs of different lengths

In order to investigate the effect of the TNTs length on their photoelectrocatalytic activity, the photocurrent density was measured. Fig.4a shows the transient photocurrent (I-t) responses of TNTs of different length under UV-vis illumination of 4 mW cm^{-2} intensity (see section 2.3) in 0.5 M Na$_2$SO$_4$ solution and at an applied voltage of +500 mV. The photocurrent response to irradiation was prompt in all cases and the current density increases with increasing TNTs length up to approximately 11 μm (TNTs30), reaching a value of approximately 420 μA cm^{-2}. Further enhancement is not observed, although the 45, 60 and 90 min TNTs have higher surface area. This suggests that both the surface area and the distance that the charge carriers have to cover dictate the performance of the photoelectrodes. Their higher surface area is also shown in the cyclic voltammograms recorded in the dark (Fig.4b). The reduction current during the negative going scan followed by the reoxidation in the subsequent positive going scan, is an indirect estimation of the surface area of the photoelectrodes. Noteworthy is that the prolonged anodization in the case of the TNTs90 may however give rise to additional surface and deep level states, which increase charge carriers' recombination rate [44] and reduce the electroactive surface area as well. As the maximum anodization time is exceeded (>60 min), secondary reactions may take place rather than oxide dissolution and growth of the nanotubes, or the solution is depleted of reactants [26].

Fig.4c shows the current density vs. applied electrode potential characteristics of TNTs of different lengths, recorded with a potential scan rate of 10 mV s^{-1}, in a supporting electrolyte solution, under 4 mW cm^{-2} UV-vis illumination. In all cases, photocurrent saturation is reached after potentials above approximately +200 mV vs. SCE, as expected for an n-type semiconductor and for limiting currents due to photogenerated charge carrier migration. Additionally, a fully depleted nanotube wall is also suggested, because there is no more space available for increasing the depletion zone with increasing electrode potential, as predicted by the Gärtner model [45]. An interesting feature of the presented potentiodymanic curves is the increasing current densities at potentials more negative than -250 mV vs. SCE. It can also be seen that the determination of the open circuit potential, or flat band position, cannot be estimated. These results are closely related to the surface area of the nanotubes and the dark

current densities given in Fig.3b. It is more or less established that when titania is subjected to strongly negative potentials, it is partially and temporarily reduced [46]. The electroactive surface area (ESA) calculated from the cathodic transformation of Ti(IV)/Ti(III) is given in the inset in Fig.4b [47]. The results confirm that the ESA of the TNTs90 is significantly reduced. The unexpectedly reduced surface area of the TNTs20 sample is probably associated with the morphology of the film (not shown), which appears to have bigger cracks (ca. 5 μm) than the rest of the samples (less than 1 μm). It can also be noted that the ESA appears lower than the theoretical one, as given from the roughness factor (Table 1), indicating that the electrolyte may not fill completely the pores. On the contrary, hydrophilicity of TNTs and capillary effects indicate effective pore filling [44]. Thus, the reduced ESA may be attributed to deviations from the idealized unit cell structure considered [26] in the calculation of the roughness factor and to extensive cracking. Finally, the photocurrent densities from the chronoamperometric curves are in good agreement with the j-U curves, suggesting steady state conditions in the latter.
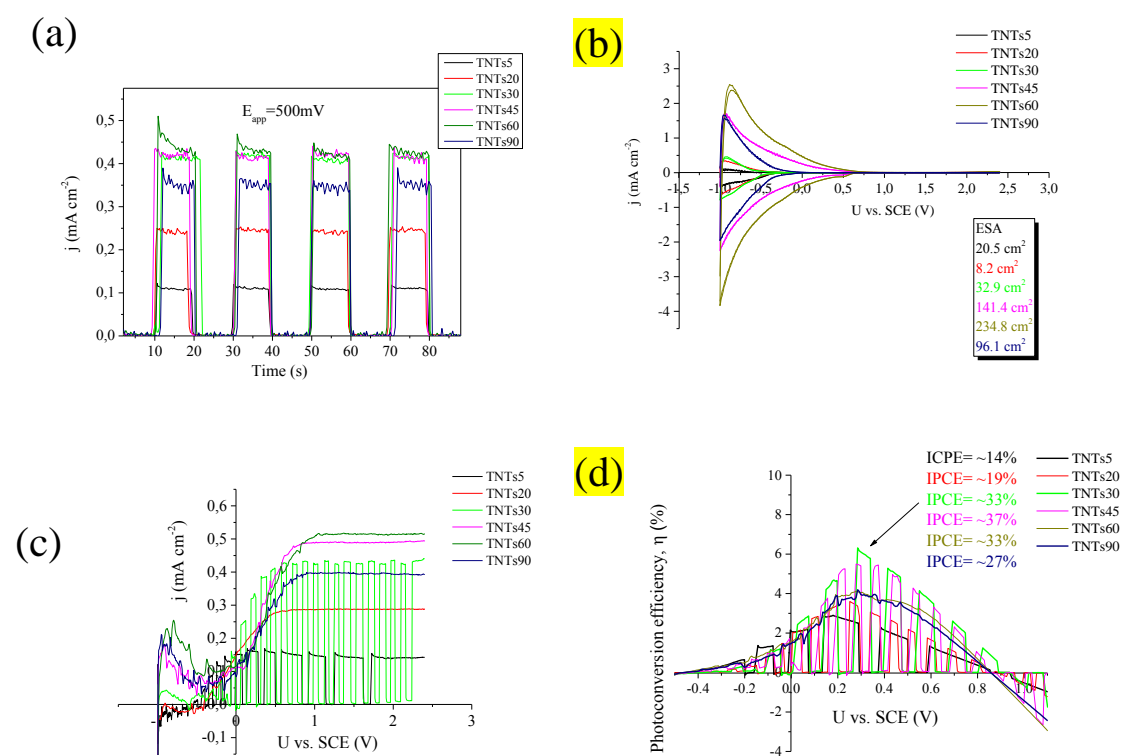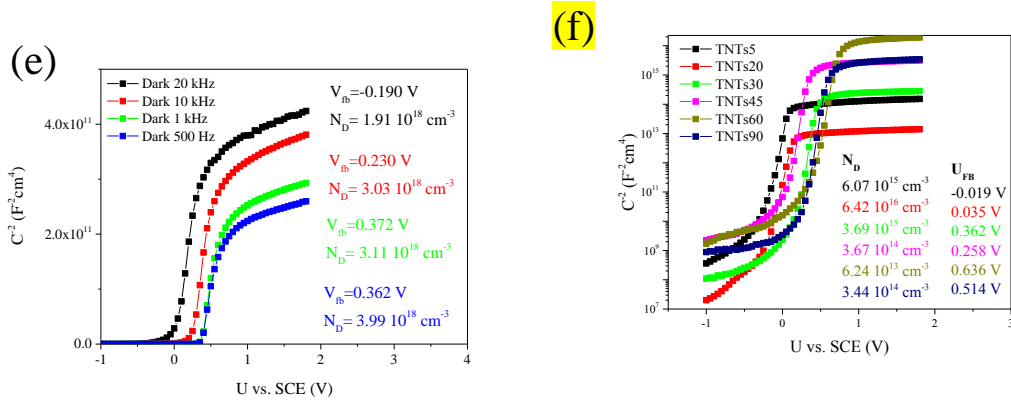
Figure 4: Photoamperometric curves (j-t) of TNTs of different lengths at an applied polarization voltage of 500 mV vs. SCE (a), cyclic voltammograms in the dark with a potential scan rate of 100 mV s^{-1}: inset shows the ESA per nominal surface area (1 cm^2) (b), j vs. U curves with light off-light on periods (c), Photoconversion efficiency, η (d). Values for incident photon-to-current efficiency (IPCE) are also given for the potential maximum. Mott-Schottky plots (e) measured in 0.5 M Na$_2$SO$_4$ electrolyte at four different frequencies (20 kHz, 10 kHz, 1 kHz, 500 Hz). Each frequency was measured under 10 mV AC imposed sinusoidal voltage and 50 mV s^{-1}. Corresponds to TNTs30. Mott-Schottky plots (f) measured in 0.5 M Na$_2$SO$_4$ at 500 Hz for TNTs of different lengths. N$_D$ values are normalized per ESA.

The variations in the photoconversion efficiency with the electrode potential are given in Fig. 4d, calculated by equations (2) and (3), as given below.

$$\eta = \left(\frac{total\ power\ output - electrical\ power\ input}{light\ power\ input}\right) x 100\% = j_p \left(\frac{E^0_{rev} - |E_{app}|}{I_0}\right) x 100\% \qquad (2)$$

where j_p is in mA cm^{-2}, and E^0_{rev} is the standard reversible potential for water splitting (1.23 V/NHE). The applied potential (E_{app}) is the difference between the electrode potential of the working electrode (vs. cathode) under illumination (E_{meas}) and that under open circuit conditions (E_{aoc}) [34], and I$_0$ is the wavelength dependent intensity of incident light in mW cm^{-2}. The incident photon-to-current efficiency (IPCE) is given for the potential of maximum η by:

14

$$IPCE(\%) = \frac{j_p 1240}{\lambda I_0} x 100\% \tag{3}$$

where λ is the wavelength of the incident light in nm, and the rest of the symbols have the same meaning as in equation (2).

The TNTs30 exhibits the highest photoconversion efficiency of ~6.3%, at approximately +280 mV vs. SCE. Although the highest IPCE corresponds to the TNTs45, the increase in the efficiency does not justify the 50% extra anodization time. Therefore, we conclude that the TNTs30 is the best performing photoelectrode and nanotubes around 10 μm have the optimal length and preparation time.

It should be noted that our analysis takes into account that the whole TNTs film is penetrated by light; therefore the whole tube is photo-activated. This assumption is confirmed by absorption measurements (not shown), where in all cases the absorption of light (reciprocal of the absorption coefficient) exceeded the length and Debye length (L) of the nanotubes. Additionally, electrochemical impedance spectroscopy (EIS) under illumination shows that the high frequency resistance and overall impedance of the films is reduced with increasing nanotube length (not shown) at all measured potentials (0, 250 and 500 mV), except for the TNTs90, where both resistance and overall impedance increased. These observations are further correlated with the donor densities in the Mott-Schottky analysis below.

The frequency dispersive character of the TNTs is presented in Fig.4e, where the Mott-Schottky treatment is applied at different frequencies. According to the Mott-Schottky theory the space charge layer (SPL) capacitance of a semiconductor as a function of the applied electrode potential is given by:

$$\frac{1}{C_{sc}^2} = \frac{2}{\varepsilon \varepsilon_0 q N_D}\left(U - U_{fb} - \frac{kT}{q}\right) \tag{4}$$

where ε is the dielectric constant (48 for anatase), ε_0 the vacuum permittivity, q the charge of the electron, N_D the donor density, U the applied potential, U_{fb} the flatband potential and the term kT/q is 25 mV at room temperature. As seen from Fig.4e, the frequency dependent SPL capacitance hampers the determination of the flatband potential and the donor density. It should

be noted that all electrodes show similar response and the N_D calculation refers to the nominal area of the specimens. According to a model proposed by Dutoit et al. [48], if the intercepts of the linear regime to the potential axis do not converge, then the width of the disturbed layer is much smaller than that of the SPL of the semiconductor. This means that the selected frequencies do not penetrate the whole SPL and in addition, they probe only surface states and shallow donors, following the micro-roughness of the electrode, thus reflecting uneven microscopic current distribution. This is also supported by the increasing donor densities with decreasing frequency, in which defects with longer emptying time, usually deep-lying electronic states, can be detected [49]. Oskam et al. [50] argued that it is not exclusively an effect of the porosity of the electrode, i.e. its solid-state properties, that account for the frequency dispersion, but also the conductivity of the electrolyte solution. They showed that with increasing electrolyte concentration the frequency dispersion on a microporous electrode was suppressed and vanished when they formed a semiconductor/metal electrode junction. As the reported V_{fb} and N_D values in the literature are estimated at a wide range of frequencies, their validity may be questionable.

A more accurate estimation of the donor density can be made if the capacitance is normalized by electroactive surface area. The calculated values are presented in the inset of Fig.4f. It can be seen that with higher ESA the donor density is decreasing, which suggests that the nanotubes become less defective [51]. In the case of the TNTs5 and TNTs20 samples, which have the smallest surface area and higher donors density, it can be assumed that recombination will be more pronounced, contributing to higher charge transfer resistance, which is confirmed by EIS. In the longer nanotubes impedance is lowered, donor density is decreased, therefore the charge recombination is lowered. At the same time, the decrease in the donor density limits the enhancement of photocurrent, photoconversion efficiency and IPCE. Finally, the relative flat band position has a tendency to shift to more positive potentials with lower donor densities. Thus, it can be concluded that the observed behavior of the nanotubes of different lengths is influenced by the surface area, as well as the donor density per ESA.

Future work aims at the use of electrochemical impedance spectroscopy (EIS) and deep-level transient spectroscopy (DLTS) in order to attempt flatband potential determination and discrete donor levels detection.

4. Conclusions

TiO$_2$ nanotubes prepared in ethylene glycol solutions containing small amounts of water and NH$_4$F are contaminated with C, N and F species. Under the given preparation conditions, C and N are placed interstitially in the TiO$_2$ lattice, while F in the form of [TiF$_6$]$^{2-}$ according to XPS analysis. Peaks at lower binding energies, which are usually attributed to substitutional doping, were observed in the N 1s and C 1s spectra after Ar$^+$ sputtering. These were, however, caused by the XPS sputtering process itself due to the higher sputtering yield of oxygen in TiO$_2$. The influence of the nanotubes length in the photoelectrocatalytic properties of the photoelectrodes showed that the performance was subject to both the surface area and electronic properties of the nanotubes. An optimum balance between ESA and charge carrier concentrations has been found for the TNTs of around 10 μm, taking into account the anodization time as a scale-up parameter as well. They showed a photoconversion efficiency of 6.3 % and IPCE of 32.88% under 4 mW cm^{-2} UV-vis illumination at +280 mV vs. SCE. Mott-Schottky analysis is a powerful tool for the determination of the flat band potential and donor density in a semiconducting electrode, but its simplified modeling provides only a qualitative explanation when applied to nanoporous structures, while more realistic values for the charge carrier concentrations can be obtained by normalizing the capacitance per electroactive surface area.

5. Acknowledgements

6. References

1.   A.L. Linsebigler, G. Lu, J.T. Yates, Chem. Rev., 95 (1995) 735-758.

2.   A. Fujishima, K. Honda, Nature, 238 (1972) 37-38.

3.   D. Kuang, J. Brillet, P. Chen, M. Takata, S. Uchida, H. Miura, K. Sumioka, S.M. Zakeeruddin, M. Grätzel, ACS Nano, 2 (2008) 1113-1116.

4.   Korotcenkov, G., Mater. Sci. Eng. B, **139** (2007) 1-23.

5.   C.G. Granqvist, A. Azens, J. Isidorsson, M. Kharrazi, L. Kullman, T. Lindström, G.A. Niklasson, C.G. Ribbing, D. Rönnow, M. Strømme Mattsson, M. Veszelei, J. Non-Cryst. Solids, 218 **(1997)** 273-279.

6.   P. Xiao, B.B. Garcia, Q. Guo, D. Liu, G. Cao, Electrochem. Commun., 9 (2007) 2441-2447.

7.   A. Fujishima, T.N. Rao, D.A. Tryk, J. Photochem. Photobiol. C, 1 (2000) 1-21.

8.   D. Gong, C.A. Grimes, O.K. Varghese, W. Hu, R.S. Singh, Z. Chen, E.C. Dickey, J. Mater. Res., 16 (2001) 3331-3334.

9.   V. Zwilling, M. Aucouturier, E. Darque-Ceretti, Electrochim. Acta, 45 (1999) 921-929.

10.   C.A. Grimes, O.K. Varghese, and S. Ranjan, Light, Water, Hydrogen - The Solar Generation of Hydrogen by Water Photoelectrolysis. 2008, New York: Springer Science + Business Media, LLC.

11.   G.K. Mor, K. Shankar, M. Paulose, O.K. Varghese, C.A. Grimes, Nano Lett., 6 (2006) 215-218.

12.   K. Zhu, T.B. Vinzant, N.R. Neale, A.J. Frank, Nano Lett., 7 (2007) 3739-3746.

13.   G.E. Thompson, G.C. Wood, Nature, 290 (1981) 230-232.

14.   J.M Macak, H. Tsuchiya, L. Taveira, S. Aldabergerova, P. Schmuki, Angew. Chem. Int. Edit., 44 (2005) 7463-7465.

15.   D. Kowalski, D. Kim, P. Schmuki, Nano Today, 8 (2013) 235-264.

16.   R. Asahi, T. Morikawa, T. Ohwaki, K. Aoki, Y. Taga, Science, 293 (2001) 269-271.

17. M. Takeshi, A. Ryoji, O. Takeshi, A. Koyu, T. Yasunori, Japanese J. App. Phys., 40 (2001) L561.

18. J.Y. Lee, J. Park, J.H. Cho, App. Phys. Lett., 87 (2005) 011904.

19. M. Zhao, J. Li, Y. Li, J. Wang, Y. Zuo, J. Jiang, H. Wang, Scientific Reports, 4 (2014) 7178.

20. M.C. Biesinger, L.W.M. Lau, A.R. Gerson, R.St C. Smart, Appl. Surf. Sci., 257 (2010) 887-898.

21. K.O. Iwu, A. Galeckas, S. Diplas, F. Seland, A.Y. Kuznetsov, T. Norby, Electrochim. Acta, 115 (2014) 66-74.

22. J. Gong, Y. Lai, C. Lin, Electrochim. Acta, 55 (2010) 4776-4782.

23. S. Ozkan, A. Mazare, P. Schmuki, Electrochim. Acta, 4176 (2015) 819-826.

24. K. Lee, A. Mazare, P. Schmuki, Chem. Rev., 114 (2014) 9385-9454.

25. A. Fujishima, X. Zhang, D.A. Tryk, Surf. Sci. Rep., 63 (2008) 515-582.

26. C.A. Grimes, G.K. Mor, TiO2 Nanotube Arrays: Synthesis, Properties and Applications. 2009, New York: Springer Science + Business Media.

27. S.P. Albu, H. Tsuchiya, S. Fujimoto, P. Schmuki, Eur. J. Inorg. Chem., 2010 (2010) 4351-4356.

28. J.K. Burdett, T. Hughbanks, G.J. Miller, J.W. Richardson, J.V. Smith, J. Am. Chem. Soc., 109 (1987) 3639-3646.

29. D.A.H. Hanaor, C.C. Sorrell, J. Mater. Sci., 46 (2011) 855-874.

30. D. Chen, Z. Jiang, J. Geng, Q. Wang, D. Yang, Ind. Eng. Chem. Res., 46 (2007) 2741-2746.

31. A. Masakazu, P.V. Kamat, Environmentally benign photocatalysts: Applications of titanium dioxide-based materials. 2010, New York: Springer Science + Business Media.

32. J. Lynch, C. Giannini, J.K. Cooper, A. Loiudice, I.D. Sharp, R. Buonsanti, J. Phys. Chem. C, 119 (2015) 7443-7452.

33. A.V. Emeline, V.N. Kuznetsov, V.K. Rybchuk, N. Serpone, Int. J. Photoenergy, 2008 (2008) 19.

34. W. Krengvirat, W., S. Sreekantan, A.F.M. Noor, G. Kawamura, H. Muto, A. Matsuda, Electrochim. Acta, 89 (2013) 585-593.

35. E.M. Neville, J.M.D. MacElroy, K.R. Thampi, J.A. Sullivan, J. Photoch. Photobiol. A, 267 (2013) 17-24.

36. Y. Zhao, Y. Li, C.W. Wang, J. Wang, X.Q. Wang, Z.W. Pan, C. Dong, F. Zhou, Solid State Sci., 15 (2013) 53-59.

37. P. Mazierski, M. Nischk, M. Gołkowska, W. Lisowski, M. Gazda, M. Winiarski, T. Klimczuk, A. Zaleska-Medynska, Appl. Catal. B-Environ..

38. O.K. Varghese, M. Paulose, T.J. LaTempa, C.A. Grimes, Nano Lett., 9 (2009) 731-737.

39. B. Yuan, Y. Wang, H. Bian, T. Shen, Y. Wu, Z. Chen, Appl. Surf. Sci., 280 (2013) 523-529.

40. S. Hashimoto, A. Tanaka, Surf. Interface Anal., 34 (2002) 262-265.

41. C. Di Valentin, G. Pacchioni, A. Selloni, S. Livraghi, E. Giamello, J. Phys. Chem. B, 109 (2005) 11414-11419.

42. H. Habazaki, K. Fushimi, K. Shimizu, P. Skeldon, G.E. Thompson, Electrochem. Commun., 9 (2007) 1222-1227.

43. D. Regonini, C.R. Bowen, A. Jaroenworaluck, R. Stevens, Mater. Sci. Eng. Reports, 74 (2013) 377-406.

44. L.V. Taveira, A.A., Sagüés, J.M. Macak, P. Schmuki, J. Electrochem. Soc., 155 (2008) C293-C302.

45. W.W. Gärtner, Phys. Rev., 116 (1959) 84-87.

46. A.K. Seferlis, S.G. Neophytides, Appl. Catal. B-Environ., 132–133 (2013) 543-552.

47. I. Mintsouli, N. Philippidis, I. Poulios, S. Sotiropoulos, J. App. Electrochem., 36 (2006) 463-474.

48. E.C. Dutoit, R.L. van Meirhaeghe, F. Cardon, W.P. Gomes, Berichte der Bunsengesellschaft für physikalische Chemie, 79 (1975) 1206-1213.

49. A.G. Muñoz, Electrochim. Acta, 52 (2007) 4167-4176.

50. G. Oskam, D. Vanmaekelbergh, J.J. Kelly, J. Electroanal. Chem. Interfacial Electrochem., 315 (1991) 65-85.

51. H. Tsuchiya, J.M. Macak, A. Ghicov, A.S. Räder, L. Taveira, P. Schmuki, Corr. Sci., 49 (2007) 203-210.